

# Feasibility of Metallic Structural Heat Pipes as Sharp Leading Edges for Hypersonic Vehicles

Craig A Steeves\*, Ming Y He<sup>†</sup>, Scott D Kasen<sup>‡</sup>, Lorenzo Valdevit<sup>§</sup>  
Haydn N G Wadley<sup>¶</sup> and Anthony G Evans<sup>||</sup>

April 16, 2008

## Abstract

Hypersonic flight with hydrocarbon-fueled airbreathing propulsion requires sharp leading edges. This generates high temperatures at the leading edge surface which cannot be sustained by most materials. By integrating a planar heat pipe into the structure of the leading edge, the heat can be conducted to large flat surfaces from which it can be radiated out to the environment, significantly reducing the temperatures at the leading edge and making metals feasible materials. This paper describes a method by which the leading edge thermal boundary conditions can be ascertained from standard hypersonic correlations, and then uses these boundary conditions along with a set of analytical approximations to predict the behaviour of a planar leading edge heat pipe. The analytical predictions of the thermostructural performance are verified by finite element calculations. Given the results of the analysis, possible heat pipe fluid systems are assessed, and their applicability to the relevant conditions determined. The results indicate that the niobium alloy Cb-752, with lithium as the working fluid, is a feasible combination for Mach 6 to 8 flight with a 3 mm leading edge radius.

## 1 Background

For aerodynamic reasons hypersonic vehicles require sharp leading edges, with millimeter scale radius. When the edges are that sharp, the heat flux into the structure is intense. Specifically, at Mach 6 to 8 (the highest Mach number attainable with hydrocarbon fuels) the fluid stagnation

---

\*Post-doctoral Scholar, University of California, Santa Barbara, Dept of Materials, Santa Barbara, CA 93106

<sup>†</sup>Project Scientist, University of California, Santa Barbara, Dept of Materials, Santa Barbara, CA 93106

<sup>‡</sup>Graduate Student, University of Virginia, Materials Science and Engineering Dept, Charlottesville, VA 22904

<sup>§</sup>Assistant Professor, University of California, Irvine, Dept of Mechanical and Aerospace Engineering, Irvine, CA 92697

<sup>¶</sup>Professor, University of Virginia, Materials Science and Engineering Dept, Charlottesville, VA 22904

<sup>||</sup>Professor, University of California, Santa Barbara, Dept of Materials, Santa Barbara, CA 93106

temperature,  $T_{st} > 1400$  C, exceeding the realistic upper use temperature of most materials. Because the tip must remain sharp and have a stable shape, ablative solutions are very challenging. Instead, the heat must be rapidly redistributed through the solid to enable dissipation by radiation from the largest possible area of the vehicle surface. The three primary passive options to obtain such a solution are: (i) Carbon-fiber-based composites that retain load-bearing capability at  $T \rightarrow T_{st}$ . (ii) Ultrahigh temperature ceramics (such as  $\text{HfB}_2$ ) that combine refractoriness  $T_M > T_{st}$  with large thermal conductivity at  $T \rightarrow T_{st}$ . (iii) Heat pipes which enable allowable equilibrium temperatures by providing exceptional effective thermal conductivity,  $k_{eff}$ .

This assessment addresses the performance of heat pipes incorporated within metallic leading edge structures during steady-state hypersonic cruise. The preferred configuration has a curved surface fully defined by the thickness  $t$ , the leading edge radius  $R_{le}$  and the angle  $\phi_0$  (which is the complement of the wedge half angle  $\theta$ ) at which the curved front connects to the flat radiating surface (see figure 1). The design length of the radiating surface,  $L$ , must be chosen to ensure that the materials remain below their maximum use temperature.

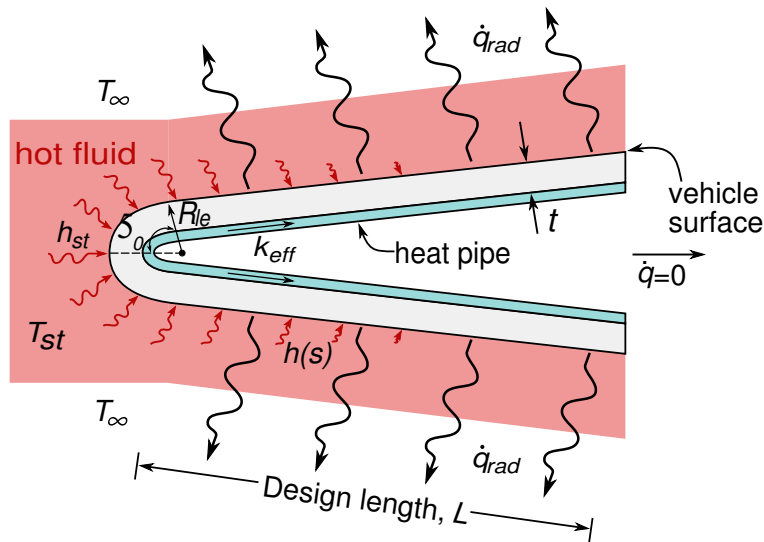


Figure 1: The local geometry and flow conditions near the leading edge.

Heat pipes have been pursued previously in the context of leading edges and other high temperature applications [see 8; 9, amongst others]. The present, structural, heat pipe differs in the sense that the design not only equilibrates the temperature but also supports transverse and shear loads (figure 2). For manufacturing facility and robustness, all-metallic designs are pursued, and their feasibility up to Mach 8 deduced.

Because of the crucial role of radiation, the temperatures induced are a strong function of

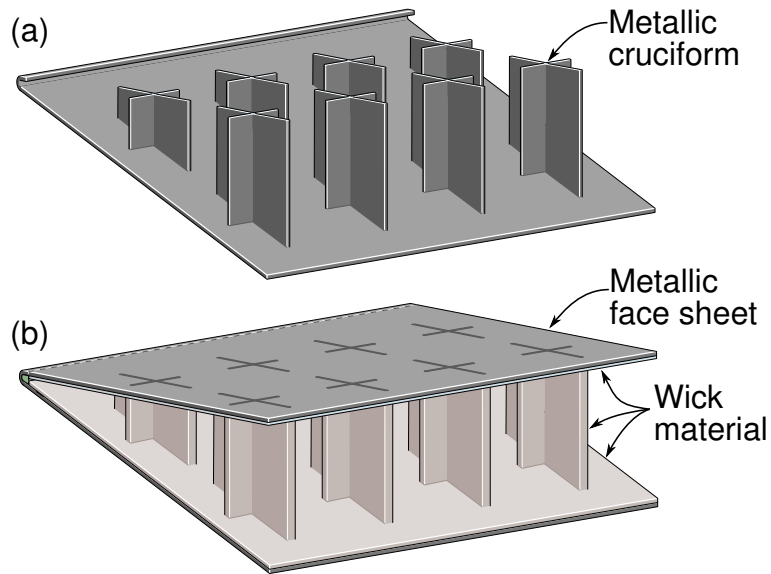


Figure 2: A structural heat pipe for the leading edge of a hypersonic vehicle showing (a) a cutaway view with the metallic wick material removed to show the cruciform structural members; and (b) the assembly, with both metallic faces and the wick installed.

the emissivity,  $\epsilon$ , of the radiating surface. While  $\epsilon$  can be quite low for conventional alloys, the refractory alloys to be explored here can be designed to have larger values by pre-oxidizing to form either alumina or silica. The most well-documented are the nickel alloys used in turbines which, when used with a bond coat, form a highly adherent, thin layer of  $\alpha$ - $\text{Al}_2\text{O}_3$  [5] with (at high temperature)  $\epsilon \geq 0.9$ .

To address this challenge, this article is structured as follows: The aerothermodynamic environment that governs the heat flux into the leading edge is characterized using procedures based on the stagnation temperature and heat transfer coefficient. Steady-state temperatures and heat fluxes induced when the heat pipe is functioning are derived using analytic approximations with the fidelity assessed using selected finite element calculations. The designs to be explored are based on nickel (Inconel 625) and niobium (Cb-752) alloys having the properties in table 1 and temperature-dependent yield strength characteristics presented in figure 3. Other refractory alloys, such as those based on molybdenum, tungsten or rhenium could be envisaged using the same basic protocol. The differing temperature and stress circumstances that arise during transients before the heat pipe begins to function are examined, as well as the influence of thin oxidation-protective coatings on the metallic surface. The operational requirements on the heat pipe are checked against models of heat pipe behavior to ensure the functionality of the system at the requisite heat flux and physical dimensions.

	Density $\rho$ (kg/m <sup>3</sup> )	Specific Heat $c_p$ (J/kgK)	Thermal Conductivity $k$ (W/mK) (@ 800 C)	Thermal Expansion $\alpha$ (ppm/K) (@ 800 C)	Young's Modulus $E$ (GPa) (@ 800 C)
Inconel 625	8440	525	21	15	155
Cb-752	9030	281	48	7.4	110

Table 1: Relevant material properties of nickel-based superalloy Inconel 625 and niobium alloy Cb-752. The temperature dependent material properties are taken at 800 C.

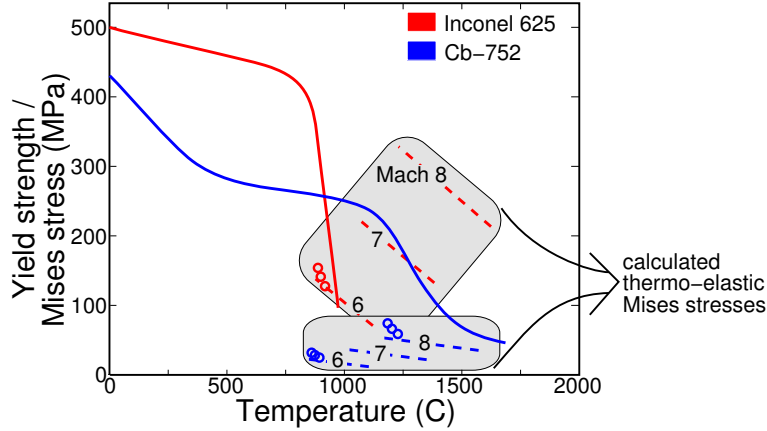


Figure 3: The temperature dependence of the yield strength for the two refractory alloys, Inconel 625 and Cb-752, used in the analysis, shown as solid lines. Analytical cross-plots of maximum stress as a function of temperature are presented as dashed lines for Mach 6 to 8. The corresponding finite element results are plotted as circles.

## 2 The Leading Edge Aerothermodynamic Environment

**Stagnation Conditions.** For hypersonic vehicles powered by scramjet engines with hydrocarbon fuels, the Mach number at cruise ranges between 6 and 8. The relation between Mach number and altitude is determined by requiring that the vehicle fly at a constant dynamic pressure (typically 48 kPa [10]). For each altitude, the free stream temperature  $T_\infty$ , pressure  $P_\infty$  and density  $\rho_\infty$  are found in standard atmosphere tables [3], summarized in table 2.

The total free stream enthalpy  $H_\infty$  is related to the temperature and vehicle velocity,  $u_\infty$ , by:

$$H_\infty = c_p T_\infty + u_\infty^2 / 2, \quad (1)$$

where  $c_p = 1.04 \text{ kJ/kgK}$  is the specific heat of quiescent air. The pressure at the stagnation point is obtained by assuming that the kinetic energy of the fluid is converted completely to pressure, and that  $P_{st} \gg P_\infty$  [1]:

$$P_{st} \approx \rho_\infty u_\infty^2 \quad (2)$$

Mach No	Altitude (km)	Temp $T_\infty$ (K)	Pressure $P_\infty$ (Pa)	Density $\rho_\infty$ (kg/m <sup>3</sup> )	Velocity $u_\infty$ (km/s)	Enthalpy $H_\infty$ (MJ/kg)	Stagnation Temp $T_{st}$ (K)
6	26.93	223.5	1900	0.0296	1.54	1.80	1651
7	28.98	225.5	1396	0.0215	2.11	2.16	2122
8	30.76	227.3	1069	0.0160	2.42	2.86	2627

Table 2: Atmospheric properties and calculated stagnation conditions for flight over the range of Mach 6 to 8 with constant dynamic pressure of 48 kPa.

The stagnation temperature can be found using a Mollier diagram [13] which is implemented in the Hypersonic Airbreathing Propulsion (HAP) software [10]. The results are summarized in table 2.

**Heat Flux.** Herein is a strategy for determining the aerothermal loading. The premise is that the air close to the surface at the leading edge reaches the full gas stagnation temperature. Heat enters the leading edge at a rate governed by a spatially varying heat transfer coefficient. A heat pipe on the back surface of the leading edge transfers the heat to a flat region, from which the heat is then radiated into low temperature space (figure 1). The system is heat balanced, such that the total heat entering the vehicle through convection is equal to that leaving by radiation. The following describes how to calculate the heat transfer coefficient and heat flux.

Fay and Riddell [7] use the results of Lees [12] to ascertain correlations for the heat flux at the stagnation point. Sutton and Graves [16] approximate these by:

$$\dot{q} = (H_g - H_w) K \sqrt{\frac{P_{st}}{R_{le}}} \quad (3)$$

where  $H_g$  is the local fluid enthalpy,  $H_w$  is the local wall enthalpy and  $K$  is a heat transfer factor which is a function of molecular weight, the mass fractions of the constituent gases, and a gas-dependent transport parameter. Sutton and Graves [16] use the results of Svehla [17] to calculate  $K = 3.6 \times 10^{-4} \text{m}^{-1} \text{kg}^{-1/2}$  for air. For the Mach numbers under investigation,  $H_g \gg H_w$ ; consequently, by setting  $H_w = 0$  and  $H_g \approx H_\infty$ , equation (3) becomes the ‘‘cold wall’’ heat flux. At the stagnation point:

$$\dot{q}_{cw,st} = H_\infty K \sqrt{\frac{P_{st}}{R_{le}}}. \quad (4)$$

The heat transfer coefficient at this location  $h_{st}$  can be approximated through:

$$h_{st} = \dot{q}_{cw,st} / T_{st}, \quad (5)$$

which varies around the curved leading edge as:  $h(\phi) = h_{st} \cos(\phi)$ . Beyond the curved section, the heat transfer coefficient declines as  $h(s) \sim 1/\sqrt{s}$ , calculated as shown in figure 4. The actual

vehicle surface is given by the solid line. Equating the heat transfer at the transition from the curved to flat sections, the coefficient along the radiating surface becomes:

$$h(s) = h_{st} \cos \phi_0 \frac{\sqrt{R_{le}}}{\sqrt{s \tan \theta}}. \quad (6)$$

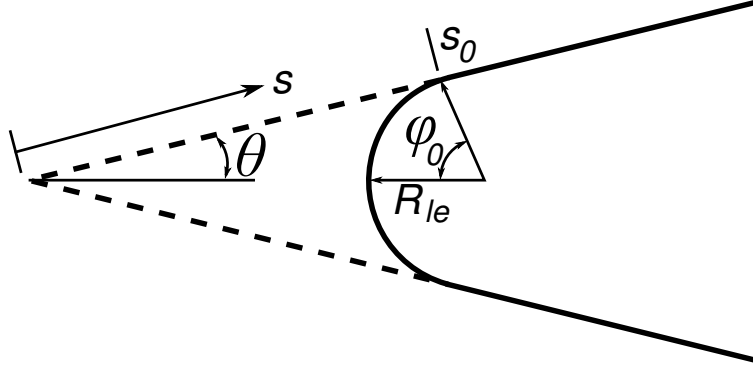


Figure 4: The assumed geometry for the calculation of the heat transfer coefficient along the flat radiating surface. The actual geometry is depicted with solid lines, while the dashed lines indicate the geometry for a perfectly sharp leading edge.

These equations permit calculation of the fluid temperature and local heat transfer coefficient around the leading edge. Implicit in this approach is the assumption that  $h$  is unaffected by the surface temperature  $T_{surf}$  and, accordingly, can be used to determine the actual heat flux once  $T_{surf}$  has been ascertained. The dependence of the stagnation point heat transfer coefficient on leading edge radius for the Mach numbers of interest is displayed in figure 5: it is independent of the material properties of the leading edge.

### 3 Steady-State Temperatures and Thermal Stresses

#### 3.1 Analytical Estimates

*Isothermal temperature.* When the heat pipe is functioning and the wall is thin, the solid approaches an isothermal temperature,  $T_{iso}$ , except very close to the leading edge. Thus,  $T_{iso}$  becomes a useful reference temperature as well as the nominal temperature of the working fluid in the heat pipe. Under this thermal condition, the system is heat balanced. The spatial extent of the solid that attains  $T_{iso}$  will be addressed later. The heat entering through the curved surface is given by:

$$\begin{aligned} Q_{in}^c &= \int_0^{\phi_0} R_{le} h_{st} \cos \phi (T_{st} - T_{iso}) d\phi \\ &\equiv R_{le} h_{st} \sin \phi_0 (T_{st} - T_{iso}). \end{aligned} \quad (7)$$

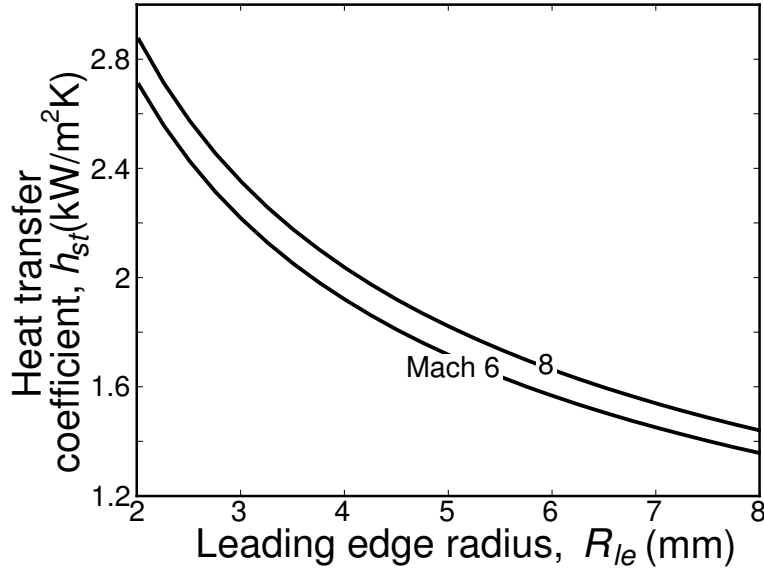


Figure 5: The stagnation point heat transfer coefficient as a function of the leading edge radius for a range of Mach numbers.

Through the flat surface the convective heat transfer is given by:

$$\begin{aligned}
 Q_{in}^f &= \int_{s_0}^{s_0+L} h(s) (T_{st} - T_{iso}) ds \\
 &\equiv \frac{2h_\phi \sqrt{R_{le}}}{\tan \theta} \left( \sqrt{R_{le} + L \tan \theta} - \sqrt{R_{le}} \right) (T_{st} - T_{iso}).
 \end{aligned} \tag{8}$$

with  $h_\phi = h_{st} \cos(\phi_0)$  and  $s$  the distance along the radiating surface as sketched in figure 4. The heat radiated out through the entire leading edge surface is:

$$\begin{aligned}
 Q_{out} &= \int_0^{L_{tot}} \epsilon \Sigma T_{iso}^4 ds \\
 &\equiv \epsilon \Sigma L_{tot} T_{iso}^4,
 \end{aligned} \tag{9}$$

where  $L_{tot}$  is the total length of the heat pipe ( $L_{tot} = R_{le} \phi_0 + L$ ) and  $\Sigma = 5.67 \times 10^{-8} \text{ W/m}^2\text{K}^4$  is the Stefan-Boltzmann constant. Heat balance requires that  $Q_{in} = Q_{out}$ , and hence:

$$\begin{aligned}
 R_{le} h_{st} \sin \phi_0 (T_{st} - T_{iso}) + \frac{2h_\phi \sqrt{R_{le}}}{\tan \theta} \left( \sqrt{R_{le} + L \tan \theta} - \sqrt{R_{le}} \right) (T_{st} - T_{iso}) \\
 - \epsilon \Sigma L_{tot} T_{iso}^4 = 0,
 \end{aligned} \tag{10}$$

which can be solved for  $T_{iso}$ . Results are plotted in figure 6(a), as a function of the length of the radiating surface, for  $R_{le} = 3\text{mm}$ ,  $\epsilon = 0.9$  and  $\theta = 6^\circ$ . Note that the isothermal temperature is sensitive to the design length  $L$  but independent of the material chosen for the system.

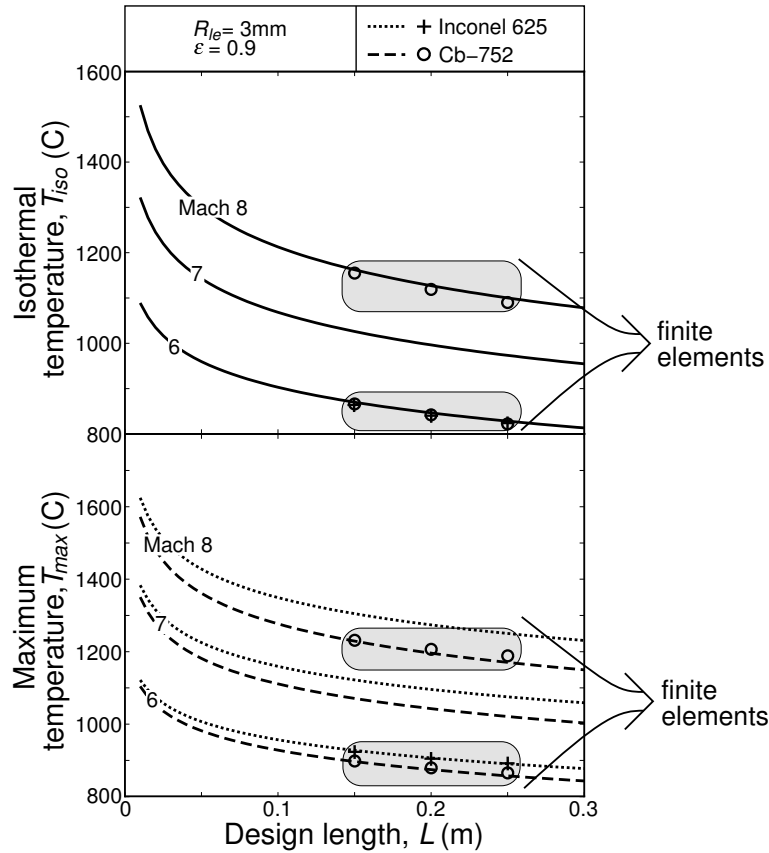


Figure 6: The leading edge temperatures calculated analytically (lines) over the relevant range of parameters, and by finite elements (circles and crosses) at Mach 6 and 8 for a vehicle with  $R_{le} = 3\text{mm}$ ,  $\epsilon = 0.9$  and  $\theta = 6^\circ$ . (a) The isothermal temperature approximation as a function of the length of the radiating surface. Note that the analytical predictions are identical for the two materials, and that the finite element calculations at Mach 6 for Inconel 625 and Cb-752 fall on top of each other. (b) The maximum temperature at the stagnation point on the surface of the leading edge for Inconel 625 (dots and crosses) and Cb-752 (dashes and circles).

**Maximum temperature.** The maximum temperature at the stagnation point can be estimated by assessing the heat flux across a small element, length  $R_{le}d\phi$  (figure 7) by using a one-dimensional calculation for heat flow into a hollow cylinder. Implicit to this estimation is that the heat flux through the wall is much larger than that along the surface (justified below). The general equation for steady-state heat conduction is:

$$k \left( \frac{\partial^2 T}{\partial r^2} + \frac{1}{r} \frac{\partial T}{\partial r} \right) = 0, \quad (11)$$

with  $k$  the thermal conductivity of the material and  $r$  the radial distance from the center. The boundary conditions are set by the stagnation temperature and heat transfer coefficient of the gas, as well as by the premise that the internal surface is at temperature  $T_{iso}$ . The solution for the

maximum material temperature at the outside surface is:

$$T_{max} = \frac{T_{iso} + T_{st} \left( \frac{R_{le} h_{st}}{k} \ln \frac{R_{le}}{R_i} \right)}{1 + \left( \frac{R_{le} h_{st}}{k} \ln \frac{R_{le}}{R_i} \right)} \quad (12)$$

where  $R_i = R_{le} - t$  is the inner radius of the leading edge. The maximum temperatures  $T_{max}$  for  $R_{le} = 3\text{mm}$ ,  $t = 1\text{mm}$  and  $\epsilon = 0.9$ , for Inconel 625 ( $k = 21\text{W/mK}$ ) and Cb-752 ( $k = 48\text{W/mK}$ ) at Mach 6 to 8, are plotted in figure 6(b) for a range of design lengths. This temperature is a function of the material thermal conductivity with higher conductivity leading to lower  $T_{max}$ . The corresponding heat flux through the surface into the heat pipe is:

$$\dot{q} = \frac{k(T_{max} - T_{iso})}{R_i \ln \frac{R_{le}}{R_i}}. \quad (13)$$

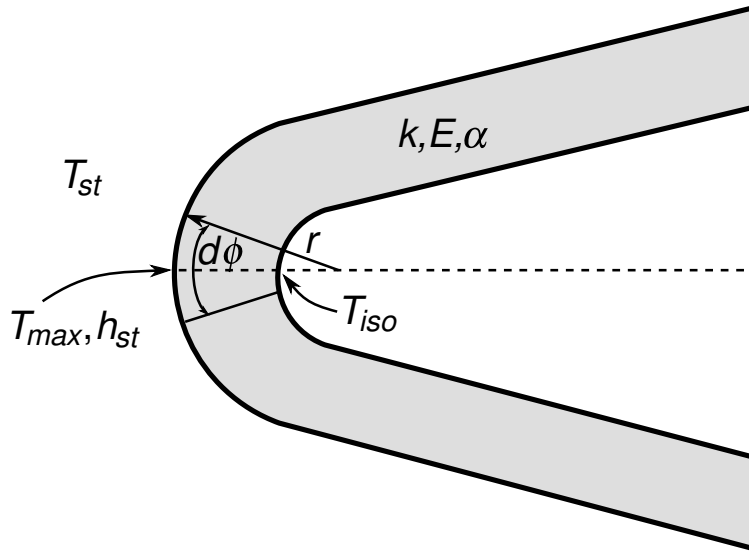


Figure 7: A sketch of the region along the stagnation line for which the temperatures are solved by a cylindrical finite difference scheme.

**Stresses.** Because the structure is metallic, the Mises stress near the leading edge (where the temperature is largest), relative to the yield strength, governs the integrity. To estimate the thermo-elastic stress (no yielding), the reference state is taken to be the long straight segment at  $T_{iso}$ . The thermal expansion misfit of the tip region, relative to this state, generates a stress. Neglecting bending (justified later), the stress is dominated by the out-of-plane strain misfit and varies through the thickness as:

$$\sigma_{eq}(r) = \alpha E (T(r) - T_{iso}), \quad (14)$$

The maximum at the exterior surface is plotted in figure 8 over the relevant range of Mach numbers. The maximum increases with larger  $L$  because, as the length increases, the total heat radiated away increases, *despite the decreased overall temperature*, requiring a larger thermal gradient at the leading edge to provide the greater heat flux. Hence, as the design length increases, the maximum temperature decreases while the maximum stress increases. Cross-plots of the relation between maximum stress and maximum temperature are shown in figure 3 for comparison with the material yield strength at that temperature. For longer design lengths (towards the left side of the graph) and lower Mach numbers, the operational conditions are clearly within the elastic envelope of the materials. However, above Mach 6, the stresses exceed the yield strength of Inconel 625 at the operating temperatures, thereby excluding this alloy from use. Conversely, Cb-752 retains its integrity even up to Mach 8, due to its combination of thermo-mechanical properties discussed below.

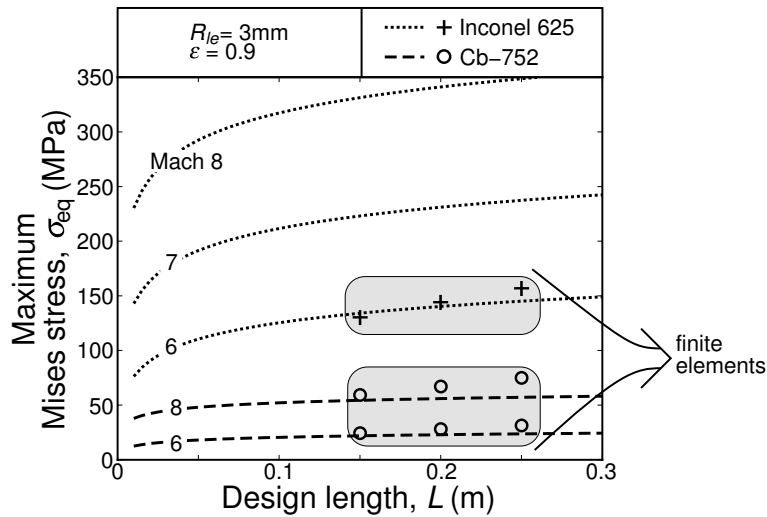


Figure 8: The maximum thermally-induced Mises stress at the exterior surface along the stagnation plane for a vehicle with  $R_{le} = 3\text{mm}$ ,  $\epsilon = 0.9$  and  $\theta = 6^\circ$ . Analytical results are lines, while finite element results are circles and crosses.

**Without a heat pipe.** In the absence of a heat pipe, heat is transferred only by longitudinal conduction along the curved region into the radiating surface resulting in the temperature distributions plotted in figure 9 for Mach 7 flight for a Cb-752 leading edge. A steep temperature gradient develops along the length and the maximum temperatures become insensitive to  $L$ . Comparison with figure 6 demonstrates the importance of having a functioning heat pipe.

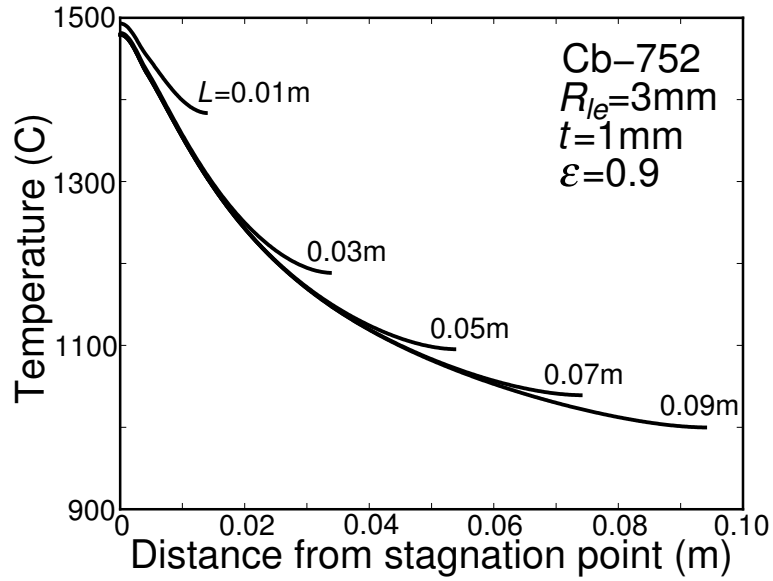


Figure 9: The behaviour of the leading edge in the absence of a heat pipe: the temperature distribution along the length of an Cb-752 ( $k = 48\text{W/mK}$ ) leading edge at Mach 7 for a range of design lengths  $L$ , assuming that the material is isothermal through the thickness and that  $\epsilon = 0.9$ ,  $R_{le} = 3\text{mm}$  and  $t = 1\text{mm}$ .

### 3.2 Finite Element Calculations

**Method.** All calculations are conducted using the commercial finite element code ABAQUS. In the analysis, 8-node coupled temperature-displacement generalized plane strain elements are used. Symmetry conditions are imposed on AD in the y-direction and on CF in the x-direction (figure 10). The solids are incorporated as an elastic/plastic medium having temperature-dependent yield strength (figure 3) with nominal strain hardening.

The external thermal boundary conditions are the same as those described in section 2. Outside the entire surface, the air is assigned the stagnation temperature, with a heat transfer coefficient that varies spatially over  $\phi$  and  $s$ . This temperature difference with that computed for the solid surface,  $T_{surf}$ , then governs the inward heat flux. Radiation to ambient  $T_{\infty}$  from the surface, at  $T_{surf}$ , determines the outward heat flux. ABAQUS simultaneously solves for the net flux and  $T_{surf}$ , as well as the Mises stresses and (when yielding occurs) equivalent plastic strains. Conduction through the solid is characterized by a (temperature invariant) thermal conductivity,  $k$ . The action of the internal heat pipe is simulated by imposing a thin (1mm) compliant layer on the inside having exceptional effective thermal conductivity,  $k_{eff}$  (figure 1). Effective thermal conductivities in excess of 100 times that of solid copper have been reported [15]. A conservative value of  $k_{hp} = 3\text{kW/mK}$  was used in all simulations. The thermo-elastic properties of Inconel 625 and Cb-752 used in the calculations are those presented in table 1 and figure 3. Results are presented

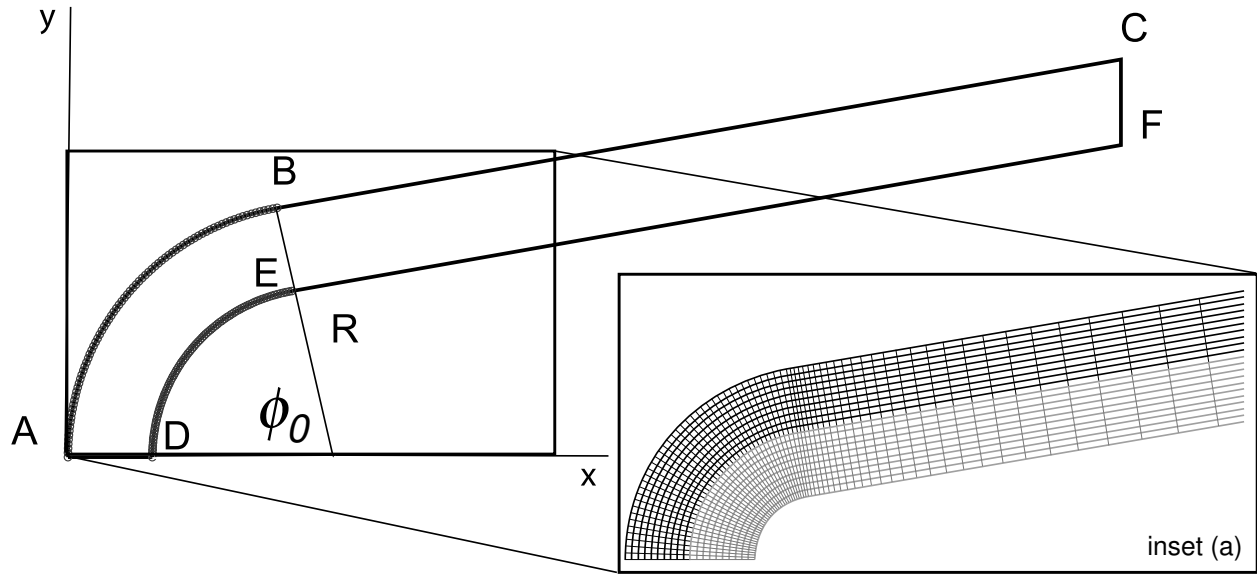


Figure 10: A typical finite element mesh used in the simulations. The solid metallic component is represented in black, while the heat pipe is grey.

for a leading edge with radius  $R_{le} = 3\text{mm}$  and wedge half-angle  $\theta = 6^\circ$

**Temperatures and heat fluxes.** In order to compare with the analytic estimates, the temperatures have been obtained for the nickel alloy at Mach 6 and the niobium alloy at Mach 6 and 8 (as a function of design length). Representative temperature distributions are plotted on figures 11 and 12 (for  $L = 0.15\text{ m}$ ). The straight sections, as well as the inside of the curved tip, are at essentially uniform temperature, identified with  $T_{iso}$ . The outside temperature at the tip is appreciably hotter, with largest value,  $T_{max}$ , at the stagnation plane. Temperatures defined in this manner are compared with the analytic estimates on the figures. The close correspondence demonstrates the utility of the analytical approach for initial design purposes. Moreover, temperature comparisons along the flat section affirms that  $T_{iso}$  is independent of the material choice. Recalling that  $T_{iso}$  dictates the choice of the working fluid, then for a 3 mm radius, at Mach 6, either sodium or potassium should be applicable, while at Mach 8, lithium would be preferred, as elaborated later.

The corresponding heat fluxes are summarized on figures 13 and 14. Those at the external surface are directed inward over the curved section but outward over most of the flat segment. Consequently, the cumulative heat input reaches a maximum just beyond the transition and declines thereafter; by definition, the net heat input is zero at the design length. The maxima are the most pertinent since these are the fluxes that must be redistributed by the working fluid in the heat pipe. These are,  $Q_{max} = 3\text{kW/m}$  at Mach 6 and  $Q_{max} = 7.6\text{kW/m}$  at Mach 8, with approximate scaling,  $Q_{max} \sim u_\infty^3$ . The contours over the curved region affirm that the flux entering the heat pipe near the

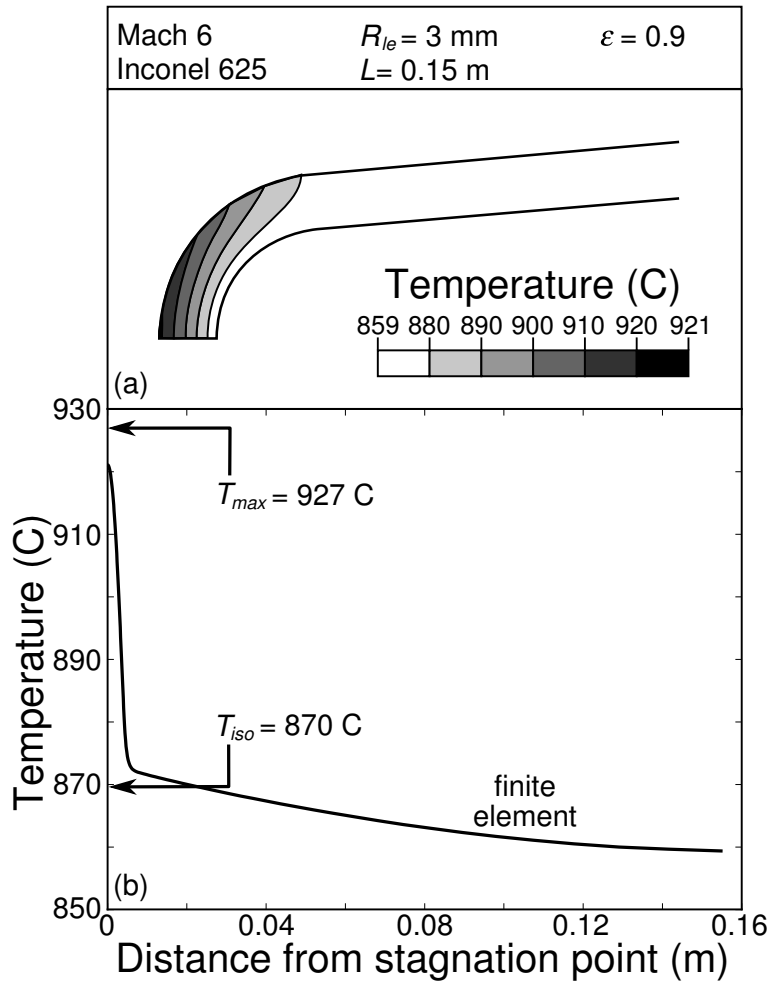


Figure 11: (a) Contours of the temperatures induced in the nickel alloy at Mach 6 when the heat pipe is functioning. (b) The temperatures along the external surface with analytic results for  $T_{iso}$  and  $T_{max}$  for  $\epsilon = 0.9$  are superimposed.

stagnation plane is largest:  $\dot{q}_{max} \approx 1.2 \text{ MW/m}^2$  at Mach 6 and  $\dot{q}_{max} \approx 3.2 \text{ MW/m}^2$  at Mach 8. (Note that these are significantly lower than the “cold wall” fluxes typically cited for leading edges at the same Mach number, altitude and radius).

**Stresses and plastic strains.** Contours of the Mises stresses are plotted on figure 15. The maxima at the tip are about 10% larger than the analytic estimates (figure 8). The difference is attributed to a small bending effect not accounted for in the analytic formula. The results for Inconel 625 (figure 15(a)) reveal that, even at Mach 6, the stresses approach the yield strength at the associated temperature (see figure 3). Indeed, the most failure susceptible element at the tip on the exterior surface is sufficiently close to yield that the safety margin would be unacceptable. The corresponding Mises stress contours for the niobium alloy (figure 15(b)) reveal much larger margins of safety, even at Mach 8. The niobium alloy is preferable because of its higher conductivity, lower

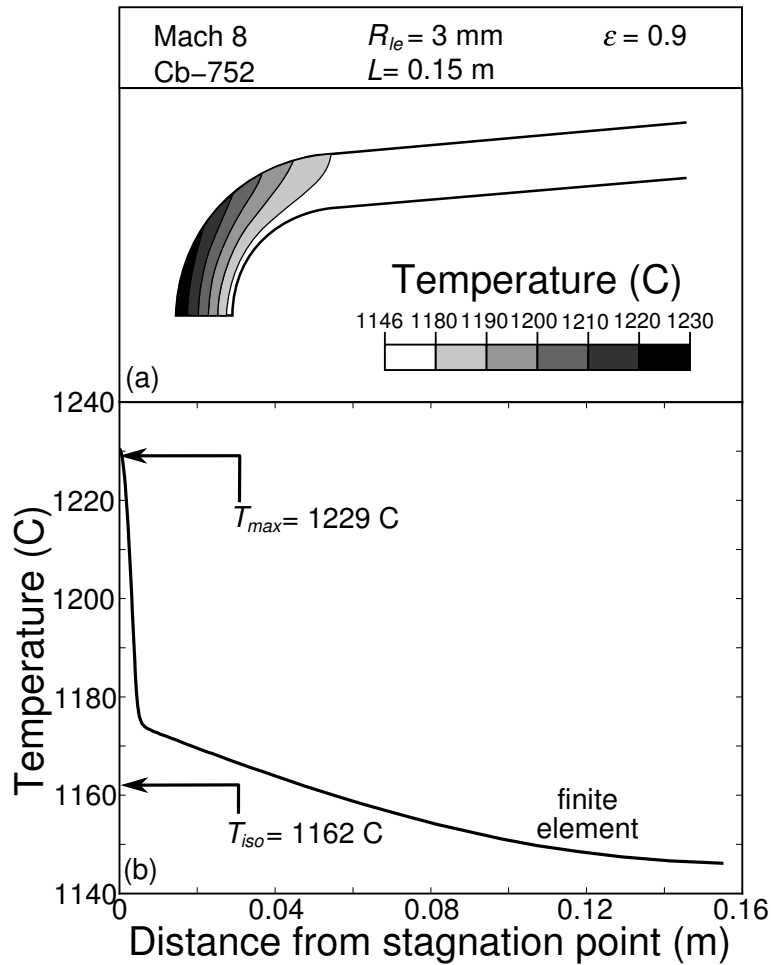


Figure 12: (a) Contours of the temperatures induced in the niobium alloy at Mach 8 when the heat pipe is functioning. (b) The temperatures along the external surface with analytic results for  $T_{iso}$  and  $T_{max}$  for  $\epsilon = 0.9$  are superimposed.

modulus and lower thermal expansion, all of which decrease the maximum stress. Coupled with greater yield strength at higher temperatures, niobium alloys are clearly a superior design choice.

## 4 Influence of Coatings and Transients

**Coatings.** The nickel and niobium alloys to be used may require oxidation protection coatings to assure multi-flight capability. This is especially true for the Nb alloys being contemplated for use at the higher Mach numbers. To examine the possible effect of these coatings on temperatures in the system, a numerical calculation has been conducted for a Mach 7 design using a Cb-752 alloy with an oxidation protection coating having thickness,  $t_{coat} = 100\mu\text{m}$ . The coating is considered to be highly insulating, with thermal conductivity,  $k = 1\text{W/mK}$ . The temperature results are summarized

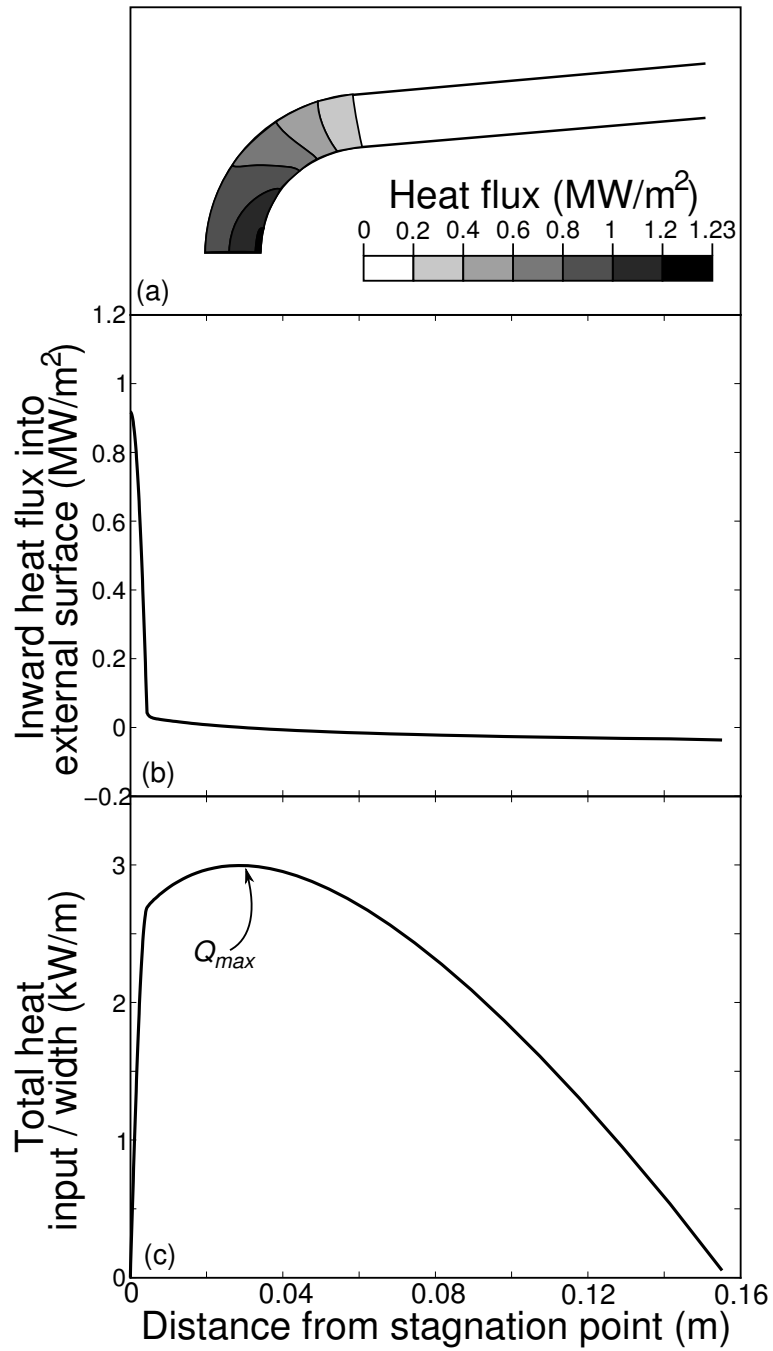


Figure 13: Heat flows at Mach 6 for an Inconel 625 leading edge. (a) Contours of heat flux at the design length  $L = 0.15\text{m}$  and  $\epsilon = 0.9$ . (b) Local heat flux into the exterior surface. (c) Integrated heat input from the leading edge. At the design length the net total heat input is zero.

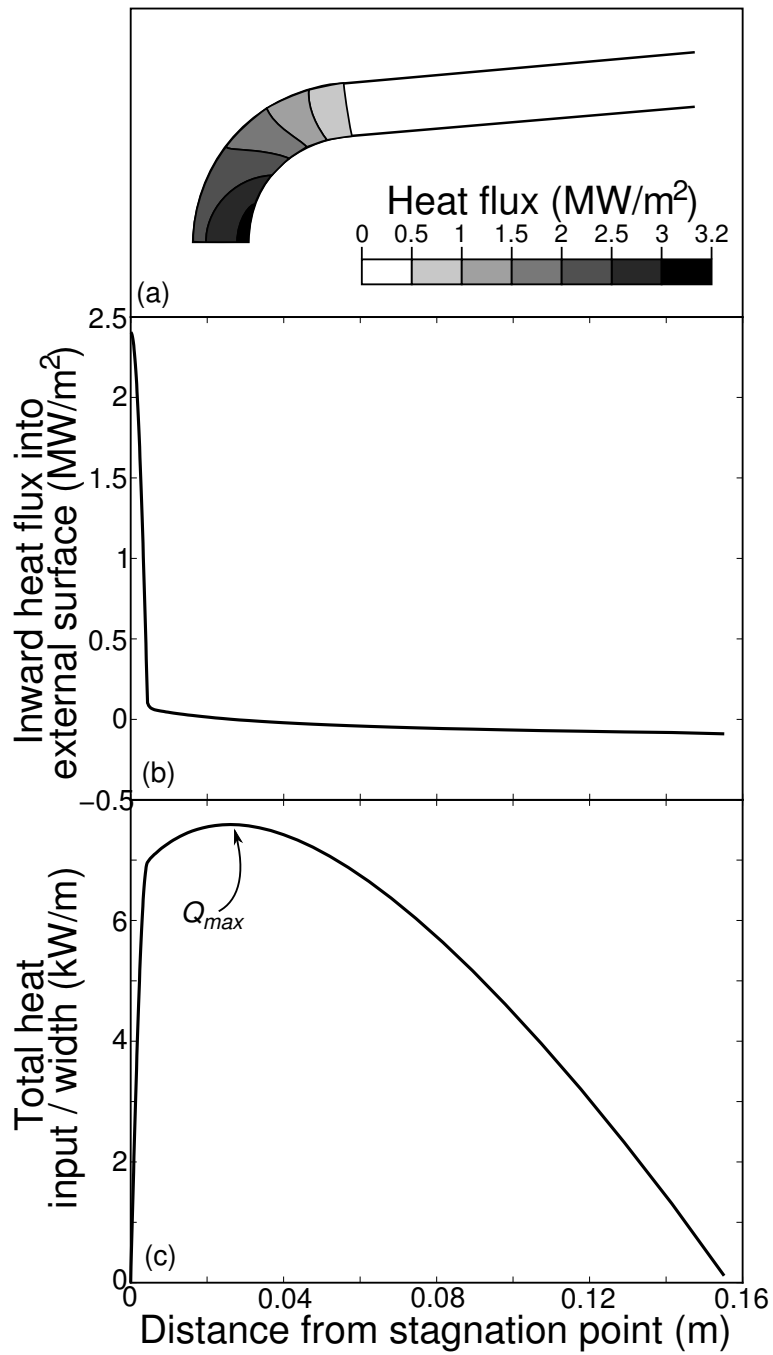


Figure 14: Heat flows at Mach 8 for a Cb-752 leading edge. (a) Contours of heat flux at the design length  $L = 0.15\text{m}$  and  $\epsilon = 0.9$ . (b) Local heat flux into the exterior surface. (c) Integrated heat input from the leading edge. At the design length the net total heat input is zero.

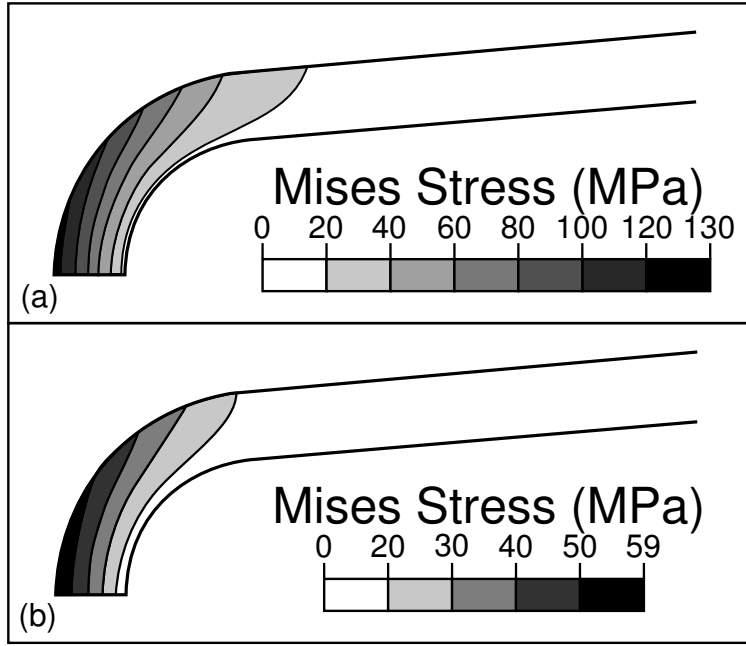


Figure 15: Mises stress and plastic strain contours when the heat pipe is functioning: (a) Mises stresses for Mach 6 with nickel-based superalloy Inconel 625; (b) Mises stresses for Mach 8 with niobium alloy Cb-752.

on figure 16. Note that the maximum temperature developed in the niobium has been reduced relative to that without the coating, but the coating surface becomes extremely hot. Moreover, a large temperature gradient is induced in the coating, with high likelihood of delamination [4]. The impact of coatings on the viability of the envisioned leading edge systems thus requires careful assessment that balances their benefits in environmental protection with their adverse susceptibility to spalling.

**Transients.** Time-dependent calculations of heat diffusion through the leading edge elucidate the transient behaviour of the system at startup. The leading edge at ambient temperature is instantaneously exposed to flight conditions. To activate the heat pipe, a minimum critical temperature,  $T_{cr}$ , must be attained at the back face; subsequently it provides heat transport dependent upon the ensuing back face temperature. The heat pipe is assumed to obey a heat flux law:

$$\dot{q} = \left( \frac{T_{bf} - T_{cr}}{T_{iso} - T_{cr}} \right)^m \dot{q}_{ss}, \quad (15)$$

where  $T_{bf}$  is the instantaneous temperature at the back face,  $\dot{q}_{ss}$  is the heat flux at the steady state, as calculated by equation 13, and  $m$  is an exponent governing the rate of heat pipe startup. Once the back face reaches  $T_{iso}$ , the heat flux in the system is in equilibrium. The time-dependent thermal behaviour of the Mach 7 Cb-752 system is shown in figure 17(a) for  $T_{cr}/T_{iso} = 0.9$  and  $m = 1$ .

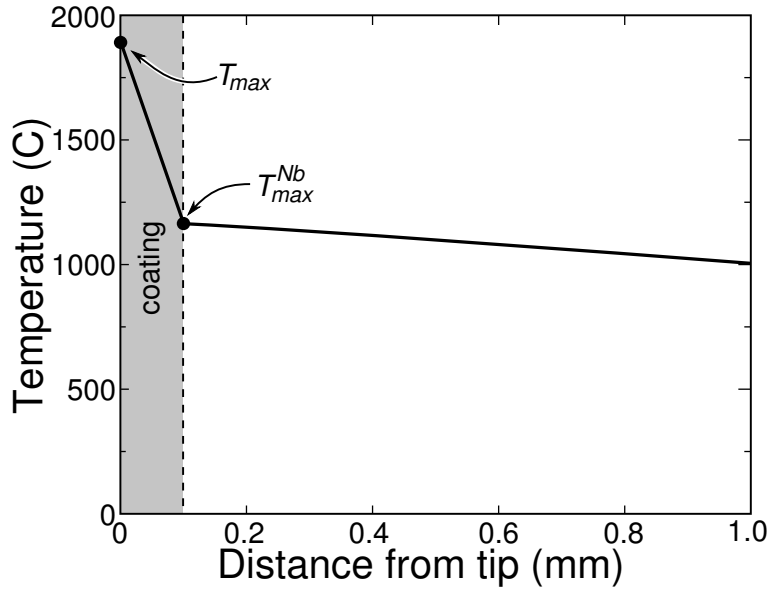


Figure 16: The temperature distribution through a niobium leading edge with a  $100\ \mu\text{m}$  anti-oxidation environmental barrier coating.

Three transient phases are evident. *Phase I*: The temperature of the outer surface rises quickly. The back face temperature rises more slowly, as heat diffuses through the thickness, causing an initial rapid stress elevation (see figure 17(b)); this phase concludes with a local maximum in stress. *Phase II*: the system moves towards thermal equilibrium. The Mises stress gradually declines because the temperature of the back face increases more quickly than the temperature of the front face. *Phase III* initiates when the heat pipe begins to operate. This activation dramatically slows the rise in back face temperature, as the Mises stress increases to a global maximum. These calculations suggest that the maximum stress during the transient phase does not exceed that at steady state. However, the results are highly dependent upon the choice of the startup temperature and the rate exponent. Experiments and detailed modeling of the heat pipe are needed to choose these accurately.

## 5 Heat Pipe Limitations

Heat pipes can fail when the heat transfer rate within the pipe is insufficient to transport the incident heat flux. Several operational phenomena affect this limit [15; 6]. Only three are relevant to the leading edge environment: (i) the *sonic limit*, encountered when the mean vapor flow velocity approaches transonic values; (ii) the *capillary limit*, which arises when the drops in liquid and vapor pressure approach the capillary pumping pressure available within the wick; and (iii) the *boiling*

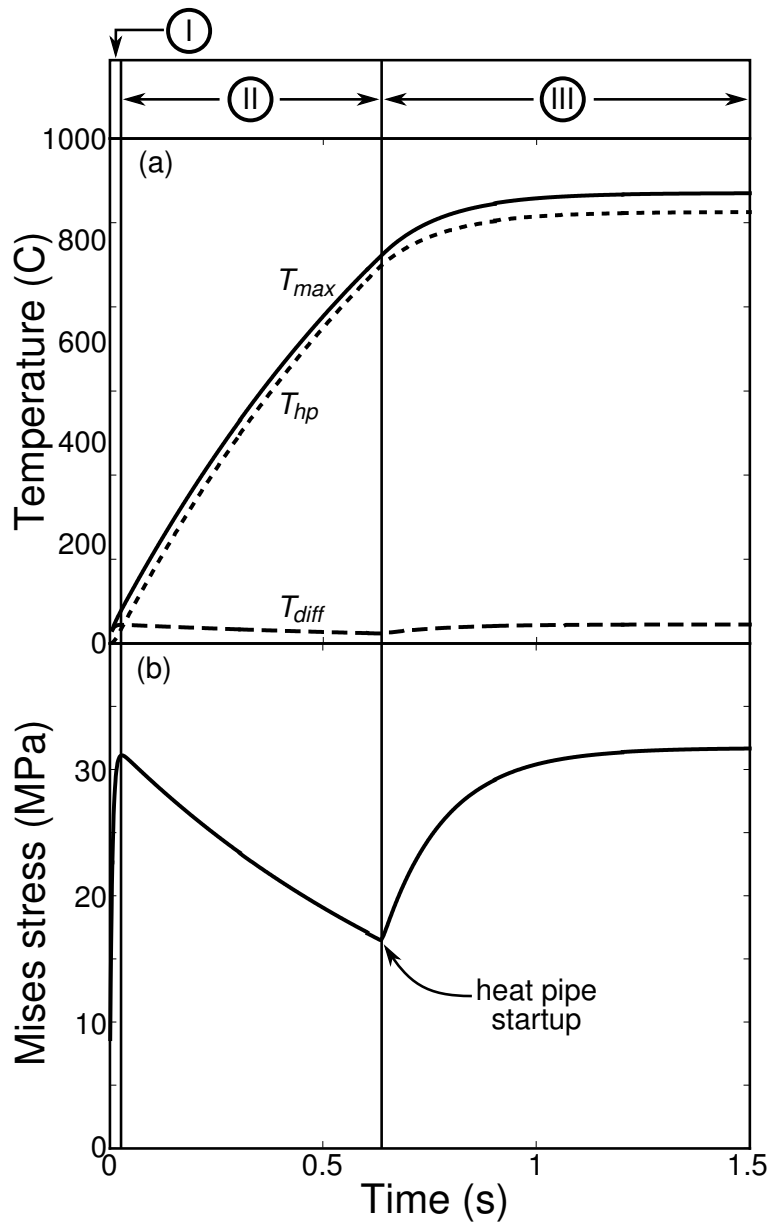


Figure 17: The idealised behaviour of the leading edge during the startup phase for a Cb-752 leading edge at Mach 7. (a) The temperature at the external surface  $T_{max}$ , at the back surface  $T_{hp}$  and the difference between the two temperatures  $T_{diff}$ . (b) The resulting Mises stress at the stagnation point.

*limit*, occurring when a critical superheating of the vapor is attained and bubbles stabilize in the wick of the evaporator zone. Detailed analyses of these phenomena which relate these limits to the thermo-physical properties of the working fluid were derived for a hollow cylindrical heat pipe [2; 15; 6], which is not directly applicable here. For the leading edge, the corresponding analysis has been conducted for the geometry depicted in figure 18, and the upper portion of the leading edge is treated as a planar heat spreader. The leading edge is constructed either from Inconel 625 with thermo-chemically compatible sodium as the working fluid, or Cb-752 with lithium as the working fluid. The wick system is a woven wire mesh of the same material as the case.

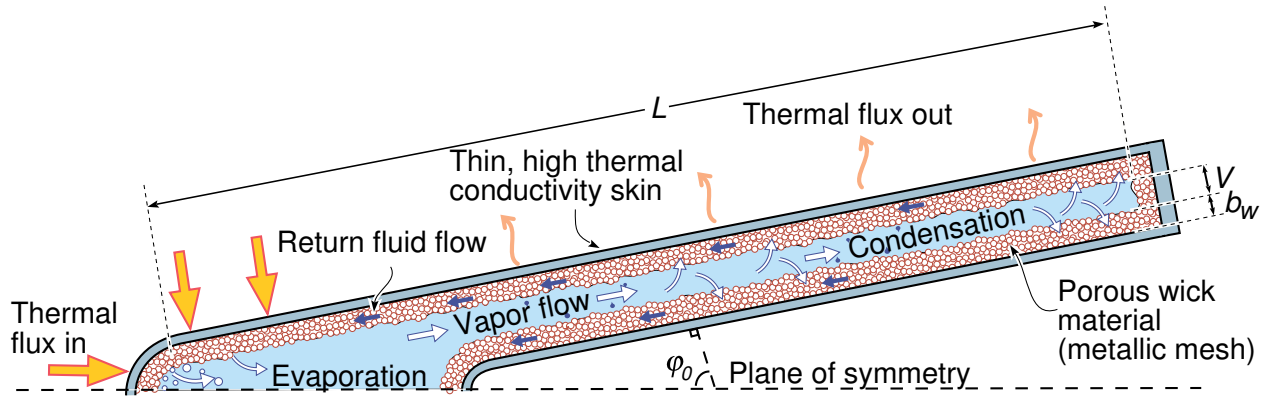


Figure 18: A cross-section schematic showing the operating principles and relevant geometry of a heat plate leading edge.

## 5.1 Sonic Limit

The sonic limit is reached when the absorbed thermal flux per unit width is given by [6]:

$$Q_{max}^{son} = V\rho_v\lambda\left(\frac{\gamma R_g T_{iso}}{2(\gamma + 1)}\right)^{1/2}, \quad (16)$$

where  $V$  is the vapor space height (see figure 18),  $\rho_v$  the vapor density,  $\lambda$  the latent heat of vaporization of the working fluid,  $\gamma$  the heat capacity ratio ( $\gamma = 1.67$  for monatomic sodium and lithium vapor), and  $R_g$  the gas constant for the vapor species within the heat pipe ( $R_{Na} = 361$  J/kgK and  $R_{Li} = 120$  J/kgK). The isothermal operating temperature of the heat pipe  $T_{iso}$  (which equals the liquid-vapor saturation temperature), is limited by the onset of rapid softening and high creep rate of the case material. Note that only at low  $T_{iso}$  is the sonic limit likely to restrict the heat transport rate.

## 5.2 Capillary Limit

The capillary limit can be derived by a pressure balance across the length of the heat pipe:

$$\Delta P_{max}^{cap} = \Delta P_l + \Delta P_v, \quad (17)$$

where  $\Delta P_{max}^{cap}$  is the maximum capillary pumping pressure, with  $\Delta P_l$  and  $\Delta P_v$  the liquid and vapor pressure drops, respectively. The additional pressure drops attributed to inertial effects upon evaporation and condensation of the working fluid are deemed negligible [6]. The maximum capillary pumping pressure is given by the Young-Laplace equation [2; 15; 6] as:

$$\Delta P_{max}^{cap} = \frac{2\sigma}{R_{eff}}, \quad (18)$$

where  $\sigma$  is the liquid surface tension and  $R_{eff}$  is the “effective pore radius” (the radius of curvature at the liquid-vapor interface in the evaporator zone), which is a function of the porous wick geometry. Its value has been experimentally determined for numerous wick structures and porosities. The assumed effective pore radius is  $R_{eff} = 1.27 \times 10^{-4}$  m, which corresponds to a woven mesh wick with  $\sim 4$  cells/mm [6].

The maximum pressure drop in the liquid within the wick can be calculated from Darcy’s model of laminar flow through a porous medium:

$$\Delta P_l = \frac{\eta_l Q_{max}^{cap}}{4\kappa b_w \rho_l \lambda} L_{tot}, \quad (19)$$

where  $\eta_l$  is the liquid dynamic viscosity,  $\kappa$  the wick permeability,  $b_w$  the wick thickness, and  $\rho_l$  the liquid density. The woven mesh wick with four unit cells per millimeter has permeability of  $\kappa = 1.93 \times 10^{-10}$  m<sup>2</sup> [6]. The absence of an adiabatic section implies that the evaporator zone length  $L_e$  and the condenser zone length  $L_c$  together occupy the entirety of the heat pipe such that  $L_{tot} = L_e + L_c$ .

When inertial forces dominate viscous forces, and the vapor is in the incompressible, laminar flow regime, as is the case here, the maximum vapor pressure drop can be derived from the governing equations describing the velocity distribution for fully developed fluid flow in a rectangular duct:

$$\Delta P_v = \frac{6\eta_v Q_{max}^{cap}}{V^3 \rho_v \lambda} L_{tot}, \quad (20)$$

where  $\eta_v$  is the vapor dynamic viscosity. Detailed derivations for turbulent and compressible flow as well as consideration of acceleration effects can be found elsewhere [11].

Substituting (18), (19), and (20) into (17) and solving for  $Q_{max}^{cap}$  gives an expression for the maximum absorbed thermal flux per unit width when constrained by capillary pumping limits:

$$Q_{max}^{cap} = \frac{4\sigma\lambda}{L_{tot}R_{eff}} \left( \frac{12\eta_n}{V^3\rho_v} + \frac{\eta_l}{2\kappa b_w\rho_l} \right)^{-1}. \quad (21)$$

Liquid sodium has a heat of vaporization two orders of magnitude lower than liquid lithium at the same temperature, suggesting that the capillary limit is particularly relevant to the sodium - Inconel system.

### 5.3 Boiling Limit

The boiling limit is reached first where the thermal flux is largest, at the point where the stagnation line intercepts the inner surface of the heat pipe wall (see figures 13(a) and 14(a)). From direct application of Fourier's Law, the boiling limit is given by:

$$\dot{q}_{max}^{boi} = \frac{k_w}{b_w} \Delta T_{crit}, \quad (22)$$

where  $k_w$  is the thermal conductivity of the saturated wick. The critical superheat,  $\Delta T_{crit}$ , is given by Faghri [6]:

$$\Delta T_{crit} = \frac{2\sigma T_{iso}}{\lambda\rho_v} \left( \frac{1}{R_b} - \frac{1}{R_{eff}} \right), \quad (23)$$

where  $R_b = 10^{-7}$  m is an order-of-magnitude estimation of the bubble radius at nucleation. The saturated thermal conductivity for a sintered woven mesh wick is given by:

$$k_w = k_l \left( \frac{k_s}{k_l} \right)^{(1-\beta)^{0.59}} \quad (24)$$

where  $k_l$  is the liquid thermal conductivity,  $k_s$  that for the solid, and  $\beta$  the wick porosity ( $\beta = 0.63$ ). The maximum heat flux at the stagnation line,  $\dot{q}_{max}$ , must be less than the allowable maximum local heat flux,  $\dot{q}_{max}^{boi}$ .

For the geometry under consideration, the heat flux into the heat pipe is not uniform. Define the evaporator length as  $L_e = Q_{max}/\dot{q}_{max}$ , where  $\dot{q}_{max}$  is the maximum heat flux entering the vapor from the heat pipe wall at the stagnation point (see figures 13(a) and 14(a)). The total heat which can be transferred from the wall to the fluid is conservatively given by:

$$Q_{max}^{boi} = \dot{q}_{max}^{boi} L_e. \quad (25)$$

## 5.4 Operational Limit Comparisons

The sonic, capillary, and boiling limits are functions of temperature-dependent thermophysical working fluid properties, namely the liquid and vapor densities, heat of vaporization, liquid surface tension, and the liquid and vapor viscosities. Values of these properties for sodium and lithium can be found in Ohse [14], resulting in the limits for the sodium / Inconel 625 and lithium / Cb-752 systems plotted in figures 19 and 20. The results in figures 13 and 14 give  $L_e \sim 2.4\text{mm}$  for both the Mach 6 and Mach 8 designs, and vapor space height  $V = 4.5\text{ mm}$  and wick thickness of  $b_w = 1\text{ mm}$  have been assumed. Both plots affirm that the heat pipes are functional under the proposed flight velocities and altitudes. While other limitations on the heat pipe operation exist, such as acoustic fluctuations due to aerodynamic loadings, they are currently beyond the purview of the standard models presented here.

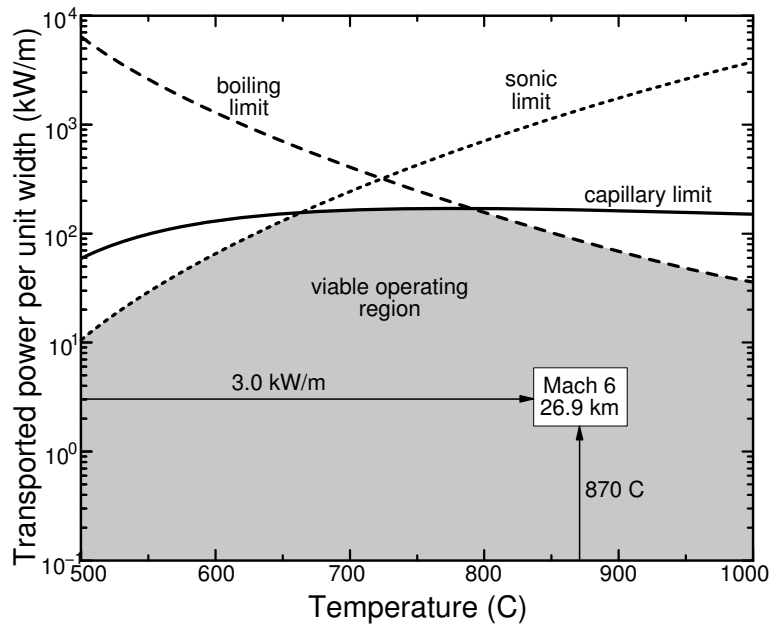


Figure 19: The predicted operational limits of a sodium - Inconel 625 heat pipe leading edge with thermal flux leading edge input corresponding to Mach 6 (26.93 km,  $\dot{q}_{max} \approx 1.2\text{ MW/m}^2$ ).

## 6 Concluding Comments

This paper contains a systematic method for calculating heat fluxes, temperatures and thermal stresses in a sharp leading edge of a hypersonic vehicle which has an integrated planar heat pipe. The boundary conditions are ascertained through the use of standard expressions involving the

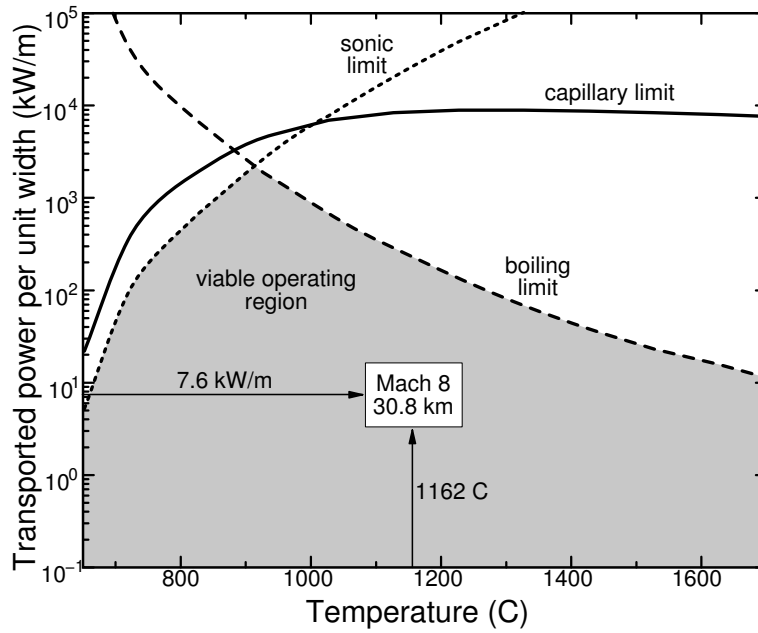


Figure 20: The predicted operating limits of a lithium - Cb-752 heat pipe leading edge with thermal flux inputs corresponding to Mach 8 (30.76 km,  $\dot{q}_{max} \approx 3.2 \text{ MW/m}^2$ ).

flight velocity and altitude, the atmospheric properties and the geometry of the vehicle. The temperatures and stresses in the leading edge are calculated using simple approximations, which are verified with finite element simulations. Conventional heat pipe estimates are then used to show the feasibility of planar metallic leading edge heat pipes. It is shown from these results that the niobium alloy Cb-752 is a better heat pipe material than the nickel alloy Inconel 625, and that a Cb-752 heat pipe with a lithium working fluid is a feasible choice for a 3 mm radius leading edge at Mach 8 or below.

The validity of the results presented here is highly dependent upon choosing the correct thermal boundary conditions. The Fay-Riddell equations are the most widely accepted technique for calculating leading edge heat flux, and the Sutton-Graves correlation is a good approximation of these results. This paper has extrapolated from the cold-wall heat flux to determine a hot-wall heat transfer coefficient. It is believed that this is a conservative extrapolation; that is, the heat transfer coefficient should not increase with decreasing temperature gradient.

The isothermal approximation used in the analysis assumes the ideal functioning of the heat pipe. This assumption cannot be validated through the finite element simulations performed here. Instead, a full model of the internal workings of the heat pipe is required, including evaporation, condensation and vapor and liquid transport. Such a model is beyond the scope of this paper. However, such validation can also be provided experimentally, so planar heat pipes are being

built and tested in a laser facility which delivers high heat flux to the leading edge. While these experiments cannot replicate the boundary conditions encountered during flight, the validity of the isothermal assumption and the expression for the maximum temperature can be ascertained by implementing the corresponding boundary conditions in the analytical models.

## Acknowledgments

The authors would like to thank Hossein Haj-Hariri of the University of Virginia Department of Mechanical and Aerospace Engineering, David Marshall of Teledyne Scientific, Vince Cuda of Swales Aerospace and George Jefferson of the Air Force Research Lab for discussions and very helpful assistance with this work. Funding has been provided by the Office of Naval Research through the MURI program Revolutionary Materials for Hypersonic Flight (Contract No. N00014-05-1-0439).

## References

- [1] J J Bertin. *Hypersonic Aerothermodynamics*. American Institute of Aeronautics and Astronautics, Washington DC, 1994.
- [2] S W Chi. *Heat Pipe Theory and Practice*. Hemisphere Publishing, Washington DC, 1976.
- [3] COESA. *U.S. Standard Atmosphere*. U.S. Government Printing Office, Washington, D.C., 1976.
- [4] A G Evans and J W Hutchinson. The mechanics of coating delamination in thermal gradients. *Surface and Coatings Technology*, 201(18):7905–7916, June 2007.
- [5] A G Evans, D R Mumm, J W Hutchinson, G H Meier, and F S Pettit. Mechanisms controlling the durability of thermal barrier coatings. *Progress in Materials Science*, 46:505–553, 2001.
- [6] A Faghri. *Heat Pipe Science and Technology*. Taylor & Francis, 1995.
- [7] J A Fay and F R Riddell. Theory of stagnation point heat transfer in dissociated air. *Journal of the Aeronautical Sciences*, 25(2):73–85, February 1958.
- [8] D E Glass, C J Camarda, M A Merrigan, and J T Sena. Fabrication and testing of Mo-Re heat pipes embedded in carbon/carbon. *Journal of Spacecraft and Rockets*, 36(1):79–86, January-February 1999.

- [9] D E Glass, C J Camarda, M A Merrigan, J T Sena, and R S Reid. Fabrication and testing of a leading-edge-shaped heat pipe. *Journal of Spacecraft and Rockets*, 36(6):921–923, November 1999.
- [10] W H Heiser and D Pratt. *Hypersonic Airbreathing Propulsion*. American Institute of Aeronautics and Astronautics, Washington DC, 1993.
- [11] S D Kasen and H N G Wadley. Unpublished research. University of Virginia, 2008.
- [12] L Lees. Laminar heat transfer over blunt-nosed bodies at hypersonic flight speeds. *Jet Propulsion*, 26(4):259–269, April 1956.
- [13] W E Moeckel and K G Weston. Composition and thermodynamic properties of air in chemical equilibrium. Technical note 4265, National Advisory Committee for Aeronautics, Lewis Flight Propulsion Laboratory, Cleveland Ohio, 1958.
- [14] R W Ohse. *Handbook of Thermodynamic and Transport Properties of Alkali Metals*, International Union of Pure and Applied Chemistry, Chemical Data Series No. 30. Blackwell Scientific, Oxford UK, 1985.
- [15] G P Peterson. *An Introduction to Heat Pipes: Modeling, Testing, and Applications*. John Wiley and Sons, New York, 1994.
- [16] K Sutton and R A Graves. A general stagnation-point convective-heating equation for arbitrary gas mixtures. Technical Report R-376, National Aeronautics and Space Administration, Langley Research Center, Hampton Virginia, 1971.
- [17] R A Svehla. Estimated viscosities and thermal conductivities of gases at high temperatures. Technical Report R-132, National Aeronautics and Space Administration, Lewis Research Center, Cleveland Ohio, 1962.